Joint mass-and-energy test of the equivalence principle at the 10^{-10} level using atoms with specified mass and internal energy

Lin Zhou,[1,*] Chuan He,[1,2,*] Si-Tong Yan,[1,2] Xi Chen,[1] Dong-Feng Gao,[1] Wei-Tao Duan,[1,2] Yu-Hang Ji,[1] Run-Dong Xu,[1,2] Biao Tang,[1] Chao Zhou,[1,2] Sachin Barthwal,[1,3] Qi Wang,[1,2] Zhuo Hou,[1,2] Zong-Yuan Xiong,[1] Yuan-Zhong Zhang,[4] Min Liu,[1] Wei-Tou Ni,[1] Jin Wang,[1,†] and Ming-Sheng Zhan[1,‡]

[1]*State Key Laboratory of Magnetic Resonance and Atomic and Molecular Physics, Wuhan Institute of Physics and Mathematics, Innovation Academy for Precision Measurement Science and Technology, Chinese Academy of Sciences-Wuhan National Laboratory for Optoelectronics, Wuhan 430071, China*

[2]*School of Physical Sciences, University of Chinese Academy of Sciences, Beijing 100049, China*

[3]*Light and Matter Physics, Raman Research Institute, Sadashivanagar, Bangalore 560080, India*

[4]*Institute of Theoretical Physics, Chinese Academy of Sciences, Beijing 100190, China*

(Received 18 May 2021; revised 9 August 2021; accepted 9 August 2021; published 26 August 2021)

We use rubidium atoms with specified mass and internal energy to carry out a joint mass-energy test of the equivalence principle (EP). We improve the four-wave double-diffraction Raman transition method (4WDR) we proposed before to select atoms with a certain mass and angular momentum state, and form a dual-species atom interferometer. By using the extended 4WDR to ^{85}Rb and ^{87}Rb atoms with different angular momenta, we measure their differential gravitational acceleration, and we determine the value of the Eötvös parameter, η, which measures the strength of the violation of EP. The Eötvös parameters of the four paired combinations $^{85}\mathrm{Rb}\,|F=2\rangle$-$^{87}\mathrm{Rb}\,|F=1\rangle$, $^{85}\mathrm{Rb}\,|F=2\rangle$-$^{87}\mathrm{Rb}\,|F=2\rangle$, $^{85}\mathrm{Rb}\,|F=3\rangle$-$^{87}\mathrm{Rb}\,|F=1\rangle$, and $^{85}\mathrm{Rb}\,|F=3\rangle$-$^{87}\mathrm{Rb}\,|F=2\rangle$ were measured to be $\eta_1=(1.5\pm3.2)\times10^{-10}$, $\eta_2=(-0.6\pm3.7)\times10^{-10}$, $\eta_3=(-2.5\pm4.1)\times10^{-10}$, and $\eta_4=(-2.7\pm3.6)\times10^{-10}$, respectively. The violation parameter of mass is constrained to $\eta_0=(-0.8\pm1.4)\times10^{-10}$, and that of internal energy to $\eta_E=(0.0\pm0.4)\times10^{-10}$ per reduced energy ratio a ($a=h\nu_0/m_i^{85}c^2$, and $\nu_0=1$ GHz). This work opens a door for joint tests of two attributes beyond the traditional pure mass or energy tests of EP with quantum systems.

DOI: 10.1103/PhysRevA.104.022822

I. INTRODUCTION

The equivalence principle (EP) is one of the basic assumptions of general relativity. Almost all new theories [1] that attempt to unify gravity with the standard model [2] require the EP to be broken. Experimental tests of EP provide opportunities for verification of different theoretical models and the emergence of new physics. Mass tests of EP have been performed in different ways, including lunar laser ranging [3], torsion balance [4,5], and satellites [6]. They have achieved a precision of 10^{-15} level [6]. EP tests using macro-objects did not apparently involve energy changes. Only with microscopic particles as test bodies can it be possible to perform an energy-dependent test of EP by selecting certain internal energy states of the particles. The early microscopic particle-based EP test was done by neutron interferometers [7,8]. In recent years, with the development of atom manipulation technology, an atom-based quantum test of EP has become possible. As listed in Table I, mass tests with atoms have been performed using ^{85}Rb - ^{87}Rb, ^{87}Rb - ^{39}K, and ^{88}Sr - ^{87}Sr atom pairs [9–16]. Beyond-mass tests have been investigated using different quantum properties, including quantum statistics [17], spin [18,19], superposition [19], and internal energy [9,15,19]. An entanglement test [20] was also proposed. All of these quantum tests use either a mass pair in a certain internal state or a state pair in a single mass.

A joint test of two attributes, such as mass and internal energy, covers the cross part (off-diagonal element) of the checking matrix, thus it would provide more information than the single attribute test. However, such two-parameter experiments are usually not easy because we need to specify and fix the attribute during the experiment. Meanwhile, we also have to alter the attribute for different combinations while keeping stable all other experimental conditions. For a quantum system, such a joint test experiment depends on the availability of quantum control techniques. The main obstacles lie in the technical complexity when putting dual-species atoms and specific quantum states together in atom interferometers (AIs). It is rather difficult to satisfy the following requirements in one experiment: (i) keeping the same specified quantum state in an AI; (ii) suppressing common mode noise for different species of atoms; and (iii) adjusting the internal energy of atoms.

Thanks to the four-wave double-diffraction Raman transition method (4WDR) we proposed before [12], by extending 4WDR to excited states here we achieve a joint EP test with specified mass and internal energy states covering an energy

*These authors contributed equally to this work.
†wangjin@apm.ac.cn
‡mszhan@apm.ac.cn

TABLE I. Mass and energy tests of the equivalence principle with atoms. ΔE is the mass-energy difference of the test pair, in units of GeV (for mass) or GHz (for internal energy, 1 GHz = 4.14 μeV). η_i is the measured Eötvös parameter. η_E is the internal energy violation parameter of reduced energy ratio a, where $a = h\nu_0/m_i^{85}c^2$ and $\nu_0 = 1$ GHz.

Mass pair	F-F'	ΔE	η_i	η_E	Ref.
^{85}Rb - ^{87}Rb	2-1	1.86 GeV	$(1.2 \pm 1.7) \times 10^{-7}$		[9]
^{85}Rb - ^{87}Rb	mixed	1.86 GeV	$(1.2 \pm 3.2) \times 10^{-7}$		[10]
^{39}K - ^{87}Rb	mixed	44.66 GeV	$(0.3 \pm 5.4) \times 10^{-7}$		[11]
^{85}Rb - ^{87}Rb	2-1	1.86 GeV	$(2.8 \pm 3.0) \times 10^{-8}$		[12]
^{39}K - ^{87}Rb	mixed @ 0g	44.66 GeV	$(0.9 \pm 3.4) \times 10^{-4}$		[13]
^{39}K - ^{87}Rb	mixed	44.66 GeV	$(-1.9 \pm 3.2) \times 10^{-7}$		[14]
^{88}Sr - ^{87}Sr	0-9/2	0.93 GeV	$(0.2 \pm 1.6) \times 10^{-7}$		[17]
^{85}Rb - ^{87}Rb	3-2	1.86 GeV	$(1.6 \pm 3.8) \times 10^{-12}$		[16]
^{85}Rb	2-3	3.04 GHz	$(0.4 \pm 1.2) \times 10^{-7}$	$(0.1 \pm 0.4) \times 10^{-7}$	[9]
^{87}Rb	$m_F = \pm 1$		$(1.2 \pm 3.2) \times 10^{-7}$		[18]
^{87}Rb	1-2	6.83 GHz	$(1.4 \pm 2.8) \times 10^{-9}$	$(0.2 \pm 0.4) \times 10^{-9}$	[19]
^{87}Rb	1-1 $\oplus$ 2		$(3.3 \pm 2.9) \times 10^{-9}$		[19]
^{87}Rb	1-2	6.83 GHz	$(0.9 \pm 2.7) \times 10^{-10}$	$(0.1 \pm 0.4) \times 10^{-10}$	[15]
^{85}Rb - ^{87}Rb	2-1	1.86 GeV + 0.00 GHz	$\eta_1 = (1.5 \pm 3.2) \times 10^{-10}$		
^{85}Rb - ^{87}Rb	2-2	1.86 GeV + 6.83 GHz	$\eta_2 = (-0.6 \pm 3.7) \times 10^{-10}$		
^{85}Rb - ^{87}Rb	3-1	1.86 GeV − 3.04 GHz	$\eta_3 = (-2.5 \pm 4.1) \times 10^{-10}$		This work
^{85}Rb - ^{87}Rb	3-2	1.86 GeV + 3.79 GHz	$\eta_4 = (-2.7 \pm 3.6) \times 10^{-10}$		
			$\eta_0 = (-0.8 \pm 1.4) \times 10^{-10}$	$(0.0 \pm 0.4) \times 10^{-10}$	

interval from micro-eV to giga-eV, in a dual-species atom interferometer. Eötvös parameters are measured for the four paired combinations, and constraints to mass and energy violation are then given (see Table I).

The significance of the joint test is that the same set of experiments within the GeV-μeV scale EP test on the two properties of mass-energy eliminate the systematic errors caused by different experiments. It should be noted that although the mass varies by 16 orders of magnitude from the energy scale so that GHz cannot add quantitatively to GeV, the values of these energies are invariant during the joint experiment, so we can still conduct experiments with only GHz scale change on the huge GeV scale background.

II. FORMULA FOR JOINT MASS-ENERGY TEST OF EP WITH ATOMS

To parametrize possible contributions of mass and energy to EP violation, we express the gravitational mass m_g of a test body as a sum of different types of mass-energy and their EP violation terms,

$$m_g = \sum_A (1+\eta^A)\frac{E^A}{c^2} = m_i + \sum_A \eta^A \frac{E^A}{c^2}, \tag{1}$$

where $m_i \equiv \sum \frac{E^A}{c^2}$ is the inertial mass, A labels different interactions, E^A are their corresponding energies, c is the speed of light, and η^A are EP violation parameters. If EP validates, then $\eta^A = 0$.

In this experiment, we use ^{87}Rb and ^{85}Rb atom pairs with different hyperfine levels. The inertial mass is equal to the sum of the mass of the lower ground state (LGS) and the internal mass-energy. Then Eq. (1) is rewritten as

$$\begin{aligned} m_g &= (1+\alpha)\frac{E^{LGS}}{c^2} + (1+\beta)\frac{\Delta E}{c^2} \\ &= (1+\alpha)m_0 + (1+\beta)\frac{\Delta E}{c^2} \\ &= m_i + \alpha m_0 + \beta\frac{\Delta E}{c^2}, \end{aligned} \tag{2}$$

where $m_i = \frac{E^{LGS}}{c^2} + \frac{\Delta E}{c^2}$ is the inertial mass, $m_0 = \frac{E^{LGS}}{c^2}$ is the rest mass of LGS, and $\Delta E = E^{\mathrm{UGS}} - E^{\mathrm{LGS}}$ is the internal energy, which is the difference between the LGS and the upper ground sate (UGS). $m_i = m_0$ because the internal energy ($\sim \mu$eV) is much smaller than the test mass ($\sim$GeV). For ^{87}Rb and ^{85}Rb atoms, Eq. (2) is rewritten as

$$\begin{aligned} m_g^{87} &= m_i^{87} + \alpha^{87} m_0^{87} + \beta\frac{\Delta E^{87}}{c^2}, \\ m_g^{85} &= m_i^{85} + \alpha^{85} m_0^{85} + \beta\frac{\Delta E^{85}}{c^2}, \end{aligned} \tag{3}$$

where α^{87} and α^{85} are the mass violation parameters of ^{87}Rb and ^{85}Rb atoms, respectively, and β is the internal energy violation parameter. ΔE is the internal energies (the difference of two hyperfine levels; the kinetic energy difference of atoms with a velocity of 2.5 m/s in the interference process is less than 0.06 μeV). We assign different mass violation parameters to account for the different composition and complex interactions within each element. The EP violation between two test bodies is described by the Eötvös parameter η,

$$\eta = 2\frac{\left(m_g^{85}/m_i^{85}\right) - \left(m_g^{87}/m_i^{87}\right)}{\left(m_g^{85}/m_i^{85}\right) + \left(m_g^{87}/m_i^{87}\right)}. \tag{4}$$

Inserting Eq. (3) into Eq. (4), taking the denominator approximately equal to 1, we get the Eötvös parameters of the four

paired combinations as

$$\begin{aligned}\eta_1 &= \eta_0,\\ \eta_2 &= \eta_0 - \beta\varepsilon^{85},\\ \eta_3 &= \eta_0 + \beta\varepsilon^{87},\\ \eta_4 &= \eta_0 + \beta(\varepsilon^{87} - \varepsilon^{85}),\end{aligned} \tag{5}$$

where ε^{85} and ε^{87} are dimensionless energy scaling factors, and β is the violation parameter of internal energy. We use parameter η_E to represent the violation parameter of reduced energy ratio a, where $\eta_E = \beta a$ and $a = h\nu_0/m_i^{85}c^2 = 5.22 \times 10^{-17}$ (m_i^{85} is the inertial mass of ^{85}Rb atoms, $\nu_0 = 1$ GHz). The values of ε^{85} and ε^{87} are listed as follows:

$$\begin{aligned}\varepsilon^{85} &\equiv \frac{\Delta E^{85}}{m_{i0}^{85}c^2} = 3.04a,\\ \varepsilon^{87} &\equiv \frac{\Delta E^{87}}{m_{i0}^{87}c^2} = 6.67a,\\ a &= \frac{h\nu_0}{m_{i0}^{85}c^2}, \quad \nu_0 = 1\ \text{GHz}.\end{aligned} \tag{6}$$

III. 4WDR-e SCHEME

We proposed and implemented the 4WDR scheme in our previous EP test [12] as shown in Fig. 1(a). The 4WDR dual-species AI has the advantage of symmetrical-recoil double-diffraction [21,22], common mode noise rejection, and a magic intensity ratio (MIR, which means the total ac Stark shift caused by Raman beams in dual-species Raman transitions is canceled to zero). However, the actual 4WDR AI needs to apply a blow away pulse to clear the remaining atoms in the middle path [as shown in the upper part of Fig. 1(b)], which is not suitable for preparing UGS (^{85}Rb $|F = 3\rangle$ or ^{87}Rb $|F = 2\rangle$) AI. To prepare UGS AI, as shown in the lower part of Fig. 1(b), an additional π-blow away pulse sequence is applied to prepare the initial state and to select narrow velocity atoms, and a repumping pulse is added to make the intermediate path atoms deviate from the interference loop. At the end of interference, a blow away pulse is used to clear UGS atoms and a repumping pulse is used to pump atoms to UGS for high contrast detection. In addition, to ensure the synchronization of the dual-species atoms and reduce the systematic error, a π-blow away state selection-repumping pulse sequence for the preparation of the initial state and speed selection is added to the LGS (^{85}Rb $|F = 2\rangle$ or ^{87}Rb $|F = 1\rangle$) AI, as shown in the upper part of Fig. 1(b). By doing this, the 4WDR is extended to be applicable to both LGS and UGS, which will be called the 4WDR-e scheme hereafter. In the experiment, the composition of the state selection pulses will be different for different atom pairs. As shown in Fig. 1(a), the frequencies of the Raman lasers satisfy the conditions

$$\begin{aligned}\omega_1 + \delta_1 &= \omega_2 + \delta_2\\ &= \omega_3 - 3.04\ \text{GHz}\\ &= \omega_4 - 6.83\ \text{GHz},\end{aligned} \tag{7}$$

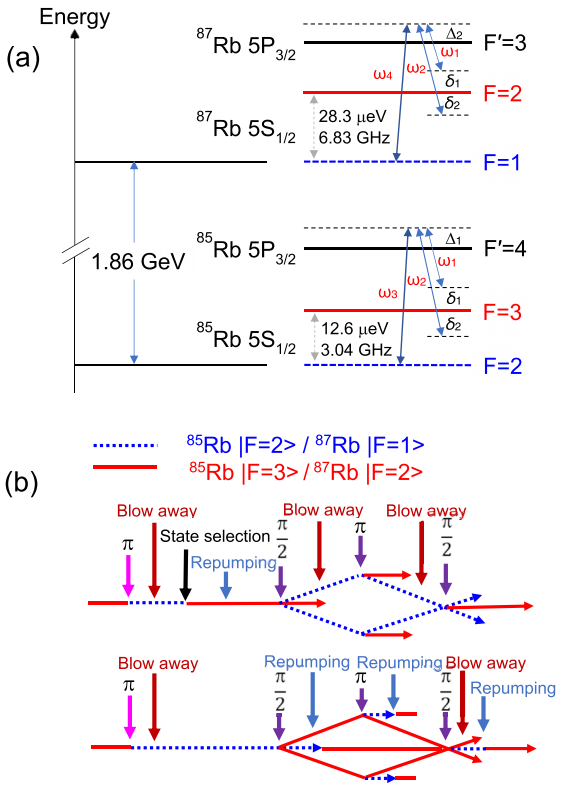

FIG. 1. Schematic diagram of 4WDR-e ^{85}Rb - ^{87}Rb dual-species AI. (a) Relevant sublevels covering the energy interval from micro-eV to giga-eV. Raman lasers with frequencies of ω_1, ω_2, and ω_3 are used for ^{85}Rb atoms, while those with frequencies ω_1, ω_2, and ω_4 are for ^{87}Rb atoms; δ_1 is the detuning of ω_1, δ_2 is the detuning of ω_2. ω_1 and ω_2 are detuned to the blue side of transitions ^{85}Rb $|F = 3\rangle$ to $|F' = 4\rangle$ with a detuning of Δ_1, and ^{87}Rb $|F = 2\rangle$ to $|F' = 3\rangle$ with a detuning of Δ_2. (b) The 4WDR-e configuration for ^{85}Rb - ^{87}Rb dual-species AI. The blue dashed lines represent LGS atoms, and red solid lines represent UGS atoms.

where δ_1 and δ_2 ($\delta_1 = -\delta_2$) are two-photon detunings of ω_1 and ω_2, respectively. The phase shift of a dual-species AI is

$$\Delta\phi = \Delta k_{\text{eff}} g(T + 2\tau)T(1 + 4\tau/\pi T), \tag{8}$$

where Δk_{eff} is the difference of effective wave vectors of the dual-species atoms, and τ is the duration of the $\pi/2$ Raman pulses. As shown in Figs. 3(a) and 3(b) in Ref. [12], the ac Stark shift caused by Raman lasers can be eliminated by selecting the frequencies and optimizing the intensity ratio of the Raman lasers. The common-mode phase noise caused by shared ω_1 and ω_2 can be rejected. The phase noise of ω_3 and ω_4 is suppressed by a double-diffraction Raman transition. The interference path in 4WDR AI is completely symmetrical, and the influence of the coupling between photon recoil and gravity gradient can be decreased to a large extent. In addition, the interference loop for one species atom remains at the same internal state, thus systematic errors (such as ac Stark shift) due to different internal states are also reduced.

The 4WDR-e scheme is explained here by taking ^{85}Rb atoms as an example. For LGS AI, the π-blow away

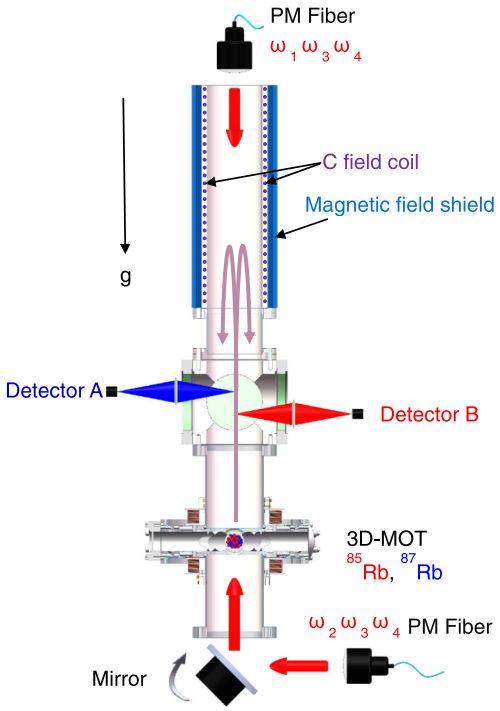

FIG. 2. Schematic diagram of dual-species AI and experimental setup. Experimental setup and process. PM: polarization maintaining; C field coil: constant-field coil.

π-repumping pulses are added for state preparation and velocity selection. The atoms in the interference loop are kept in the $|F = 2\rangle$ state by performing upward and downward recoil operations on the atoms at the same time. During coherent operation, the atoms remaining in the $|F = 3\rangle$ state will affect the interference. Therefore, a blow away pulse is added to clear atoms in the $|F = 3\rangle$ state.

For UGS AI, the π-blow away pulses are added for state preparation and velocity selection. After the atoms interact with the first $\pi/2$ pulse, they are transited from $|F = 2\rangle$ to $|F = 3\rangle$. A repumping pulse is used to pump the atoms from $|F = 2\rangle$ to $|F = 3\rangle$. Although this process cannot completely clean up the atoms in the $|F = 2\rangle$ state, it can ensure that they are only in the background without participating in the interference process. Due to the presence of a repumping pulse, the atom number in the background increases sharply. To decrease the background, we use a blow away repumping pulse sequence after the last Raman $\pi/2$ pulse, and we only detect the atoms in the $|F = 2\rangle$ state that participate in the interference loop. Note that, for atomic interferometers in ^{85}Rb $|F = 2\rangle$ and ^{87}Rb $|F = 1\rangle$ states, since the blow away and repumping pulses used during the detection change the detected state, a correction of a π phase is required to be added to the phase shift.

IV. EXPERIMENT

A. Experimental setup and process

The experimental setup is shown in Fig. 2, which is upgraded from that in our previous work [12]. It is briefly described as follows. The three-dimensional magneto-optical trap (3D-MOT) of the lower part of the fountain is a (0,0,1) configuration. The atom cloud with a temperature of 3 μK is launched to a height of about 2 m by moving molasses. The uniform magnetic field area for the atom interferometer is >1 m. The piezoelectric ceramic mounted mirror is for scanning the angle of the Raman lasers and compensating for the Coriolis effect. A time-division-multiplexing method [23] is used to couple multiple laser beams into one fiber. A group of Raman beams (ω_1, ω_3, and ω_4) propagate downward through the top window of the vacuum chamber. Another group of Raman beams (ω_2, ω_3, and ω_4) propagate upward through the bottom window of the vacuum chamber. An active compensation is used for the magnetic field shield to further reduce fluctuation of the magnetic field. The fluorescence of ^{85}Rb and ^{87}Rb atoms is alternately collected by detector A and B to reduce errors caused by the inconsistency of the detectors. For dual-species AI with different atom pairs, atoms are initially prepared to states ^{85}Rb $|F = 3\rangle$ and ^{87}Rb $|F = 2\rangle$. The additional pulse sequences can be arranged differently. The specific pulse sequence for the four pairs is shown in Fig. 3. These pulse sequences are described in detail as follows:

(a) ^{85}Rb $|F = 2\rangle$-^{87}Rb $|F = 1\rangle$ [Fig. 3(a)]. A π-blow away π-repumping pulse sequence is applied to ^{85}Rb and ^{87}Rb for state preparation and velocity selection, after which atoms in states ^{85}Rb $|F = 3\rangle$ and ^{87}Rb $|F = 2\rangle$. Here, the π-pulse is a weak single-diffraction Raman pulse used to transfer narrow-velocity atoms. The blow away pulse is used to clear the atoms residing in states ^{85}Rb $|F = 3\rangle$ and ^{87}Rb $|F = 2\rangle$, and a repumping pulse is applied for repumping atoms from ^{85}Rb $|F = 2\rangle$ and ^{87}Rb $|F = 1\rangle$ to ^{85}Rb $|F = 3\rangle$ and ^{87}Rb $|F = 2\rangle$. A $\pi/2$-blow away-π-blow away-$\pi/2$ pulse sequence is applied to realize ^{85}Rb $|F = 2\rangle$-^{87}Rb $|F = 1\rangle$ dual-species AI. Here, the blow away pulse is used to clear the ^{85}Rb $|F = 3\rangle$ and ^{87}Rb $|F = 2\rangle$ state atoms residing in the middle path.

(b) ^{85}Rb $|F = 2\rangle$-^{87}Rb $|F = 2\rangle$ dual-species AI [Fig. 3(b)]. A π-blow away pulse sequence is applied to ^{87}Rb atoms and a π-blow away-π_c-repumping pulse sequence is applied to ^{85}Rb atoms for states preparation and velocity selection, after which atoms in states ^{87}Rb $|F = 1\rangle$ and ^{85}Rb $|F = 3\rangle$. Here the π_c-pulse, a copropagating Raman pulse, is used to transfer ^{85}Rb $|F = 2\rangle$ atoms to state ^{85}Rb $|F = 3\rangle$. The purpose of other laser pulses is the same as that described in Fig. 3(a). A $\pi/2$-blow away-π-blow away-$\pi/2$ pulse sequence is applied to realize ^{85}Rb $|F = 2\rangle$ AI, and a $\pi/2$-repumping-π-repumping-$\pi/2$ pulse sequence is applied to realize ^{87}Rb $|F = 2\rangle$ AI. Here, the repumping pulse is used to pump atoms in states ^{87}Rb $|F = 1\rangle$ to ^{87}Rb $|F = 2\rangle$, and the blow away-repumping pulse sequence clears the atoms residing in states ^{87}Rb $|F = 2\rangle$ and pumps atoms in states ^{87}Rb $|F = 1\rangle$ to ^{87}Rb $|F = 2\rangle$ for detection.

Since a copropagating Raman pulse is used for state inversion of ^{85}Rb, ω_3 needs to be reduced by 30 kHz after this pulse to compensate for the frequency shift caused by photon recoil and to satisfy the laser resonance conditions during the Raman transition.

(c) ^{85}Rb $|F = 3\rangle$-^{87}Rb $|F = 1\rangle$ dual-species AI [Fig. 3(c)]. A π-blow away-π-repumping pulse sequence is applied to

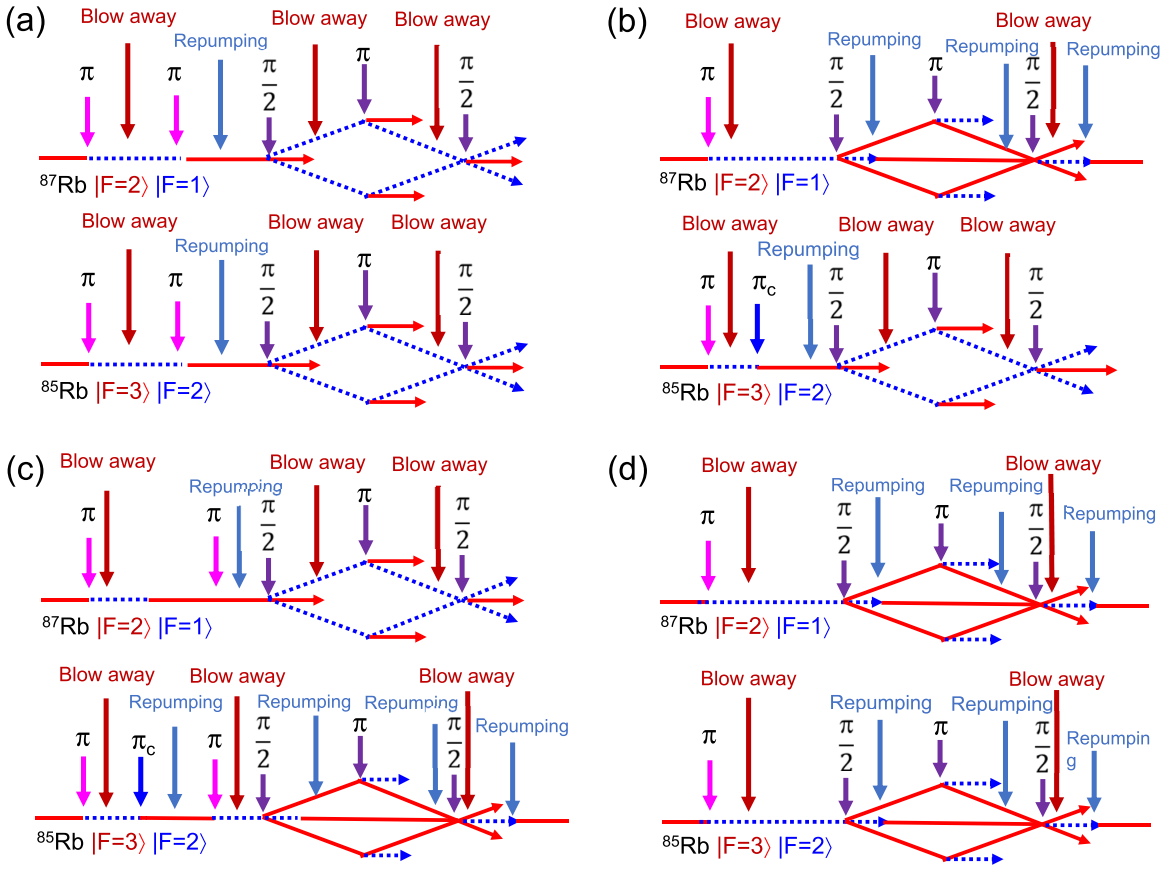

FIG. 3. Schematic diagram of 4WDR dual-species AIs with specified mass and internal energy. (a) ^{85}Rb $|F=2\rangle$-^{87}Rb $|F=1\rangle$ dual-species AI. (b) ^{85}Rb $|F=2\rangle$-^{87}Rb $|F=2\rangle$ dual-species AI. (c) ^{85}Rb $|F=3\rangle$-^{87}Rb $|F=1\rangle$ dual-species AI. (d) ^{85}Rb $|F=3\rangle$-^{87}Rb $|F=2\rangle$ dual-species AI.

^{87}Rb atoms, and a π-blow away-π_c-repumping-π-blow away pulse sequence is applied to ^{85}Rb atoms for state preparation and velocity selection. The purpose of laser pulses is the same as that described in Figs. 3(a) and 3(b). A $\pi/2$-blow away-π-blow away-$\pi/2$ pulse sequence is applied to realize ^{87}Rb $|F=1\rangle$ AI, and a $\pi/2$-repumping-π-repumping-$\pi/2$ pulse sequence is applied to realize ^{85}Rb $|F=3\rangle$ AI. The blow away-repumping pulse sequence clears the atoms residing in states ^{85}Rb $|F=3\rangle$ and pumps atoms in states ^{85}Rb $|F=2\rangle$ to ^{85}Rb $|F=3\rangle$ for detection.

Again, since a copropagating Raman pulse is used for state inversion of ^{85}Rb, ω_3 needs to be increased by 30 kHz after this pulse to compensate for the frequency shift caused by photon recoil and to satisfy the laser resonance conditions during the Raman transition.

(d) ^{85}Rb $|F=3\rangle$-^{87}Rb $|F=2\rangle$ dual-species AI [Fig. 3(d)]. A π-blow away pulse sequence is applied to ^{85}Rb atoms and ^{87}Rb atoms for states preparation and velocity selection. The purpose of laser pulses is the same as that described in Figs. 3(a) and 3(b). A $\pi/2$-repumping-π-repumping-$\pi/2$ pulse sequence is applied to realize ^{85}Rb $|F=3\rangle$-^{87}Rb $|F=2\rangle$ dual-species AI. The blow away-repumping pulse sequence clear the atoms residing in states ^{85}Rb $|F=3\rangle$ and ^{87}Rb $|F=2\rangle$, and pumps atoms in states ^{85}Rb $|F=2\rangle$, ^{87}Rb $|F=1\rangle$ to ^{85}Rb $|F=3\rangle$, ^{87}Rb $|F=2\rangle$ for detection.

B. Experimental results

The statistical uncertainty is improved (from 8×10^{-9} [12] to 6×10^{-11}) by improving atom numbers, compensating for the rotation of the Earth, increasing stability, and the free evolution time. To increase the signal-to-noise ratio and to suppress systematic errors, the z-direction effective temperature of the atoms participating in interference is lowered to 400 nK. The evolution time T among $\pi/2$-π-$\pi/2$ Raman pulses is carefully adjusted to 203.164 ms to minimize ellipse-fitting error [24,25].

The experimental data for four combination pairs are shown in Fig. 4. Figure 4(a1) shows 640 measurements of η_1 using the ^{85}Rb $|F=2\rangle$-^{87}Rb $|F=1\rangle$ atom pair, where each measurement is given by ellipse fitting (with a free evolution time of 203.164 ms and a measurement time of 280 s for two detectors). The average value of these measurements is 2.5×10^{-10}. Figures 4(a2), 4(a3), and 4(a4) show 512 measurements of η_2, η_3, and η_4 using ^{85}Rb $|F=2\rangle$-^{87}Rb $|F=2\rangle$, ^{85}Rb $|F=3\rangle$-^{87}Rb $|F=1\rangle$, and ^{85}Rb $|F=3\rangle$-^{87}Rb $|F=2\rangle$ atom pairs, respectively. The Allan deviations are shown in Fig. 4(b). The red squares are data of η_1, and the statistical uncertainty is 0.6×10^{-10} at an average time of 35 840 s. The black dots, green boxes, and blue triangles are data of η_2, η_3, and η_4, respectively. The corresponding statistical uncertainties at an average time of 17 920 s are 1.8×10^{-10}, 2.5×10^{-10}, and 1.8×10^{-10}, respectively.

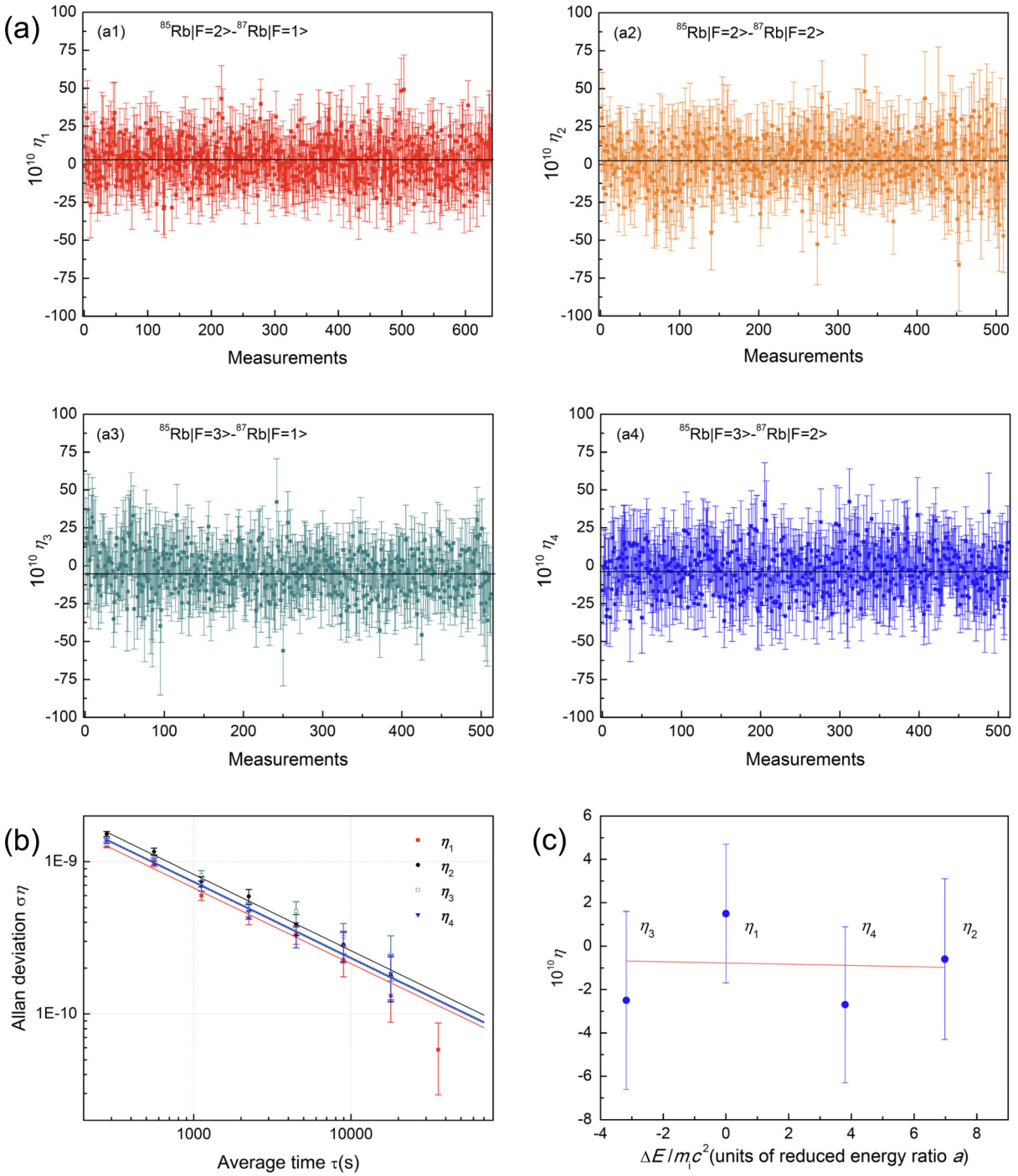

FIG. 4. Experimental data. (a) Experimentally measured η values, where the error corresponding to the effective wave vector is corrected. Parts (a1), (a2), (a3), and (a4) are measurements for η_1, η_2, η_3, and η_4, respectively. (b) Allan deviation of η_1 (red squares), η_2 (black dots), η_3 (green boxes), and η_4 (blue triangles). (c) Dependence of η values on energy, the intercept value of the fitted straight line $\eta_0 = (-0.8 \pm 1.4) \times 10^{-10}$, and the slope value $\eta_E = (0.0 \pm 0.4) \times 10^{-10}$. $a = h\nu_0/m_i^{85}c^2$ and $\nu_0 = 1$ GHz.

V. ASSESSMENT OF SYSTEMATIC ERRORS

Compared to previous work [12], the systematic errors are suppressed by correcting the wave vector, optimizing MIR, compensating for the rotation of the Raman beams mirror, calibrating the gravity gradient error, the quadratic Zeeman shift, and suppressing the wave-front error. Systematic errors are calibrated by modulation experiments and theoretical calculation. These assessments are described as follows.

A. Correction of the wave vector

The phase-shift difference between ^{85}Rb and ^{87}Rb atom interferometer is described in Eq. (8). The values of Δk_{eff} with different atom pairs are listed in Table II, where $T = 203.164$ ms, $\tau = 31\,\mu$s, and the uncertainty of the wave-

TABLE II. The values of Δk_{eff} with different test pairs.

Test pairs	(1)	(2)	(3)	(4)
Δf_{rec} (kHz)	0	30	−30	0
Δk_{eff} (m^{-1})	159.2402	159.2415	159.2390	159.2402
$\Delta\eta$ (10^{-10})	49435.6	49436.0	49435.2	49435.6

(1) $^{85}\text{Rb}\,|F=2\rangle$-$^{87}\text{Rb}\,|F=1\rangle$
(2) $^{85}\text{Rb}\,|F=2\rangle$-$^{87}\text{Rb}\,|F=2\rangle$
(3) $^{85}\text{Rb}\,|F=3\rangle$-$^{87}\text{Rb}\,|F=1\rangle$
(4) $^{85}\text{Rb}\,|F=3\rangle$-$^{87}\text{Rb}\,|F=2\rangle$

vector correction is 5×10^{-11}. The difference of Δf_{rec} is caused by the frequency change of ω_3 after applying copropagating state selection pulses.

B. ac Stark shift

The ac Stark shift is caused by Raman lasers, blow away, and repumping lasers. In our previous experiment [12], the MIR of the Raman lasers was set to $I_1 : I_2 : I_3 : I_4 = 1.0 : 1.0 : 3.1 : 14$ with an accuracy of 10%, which was limited by the fluctuation of the Raman laser intensities. The maximum residual ac Stark shift was calibrated to be 6 kHz by modulating the Raman laser intensity from 10% to 100%. To reduce the shift, the MIR of the four Raman lasers is controlled to $I_1 : I_2 : I_3 : I_4 = 1.00 : 1.00 : 3.05 : 14.3$. The long-term drift of the laser intensity is decreased to less than 2% by controlling the temperature of the optics table, feedbacking, and isolation of the vibration of optics. The shift is reduced to less than 500 Hz. The dependence of the ac Stark shift on the ratio precision is shown in Fig. 5. To estimate the influence of the ac Stark shift on η, we simulate the shift caused by Raman lasers as

$$\Delta\phi = 8\tau\left(\delta_{\text{ac}}^{\text{dw}} - \delta_{\text{ac}}^{\text{up}}\right), \tag{9}$$

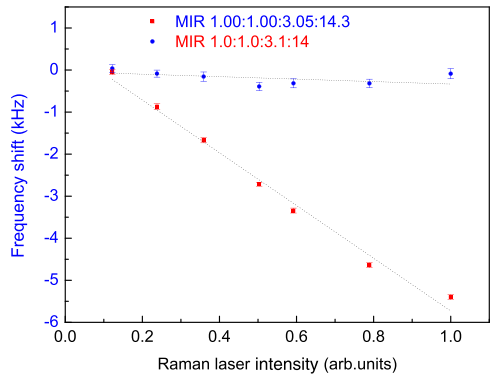

FIG. 5. Dependence of the ac Stark shift on the magic intensity ratio of the Raman lasers. MIR $= I_1 : I_2 : I_3 : I_4$, which is magic intensity ratio of four Raman beams with frequencies of ω_1, ω_2, ω_3, and ω_4. The red dots are data before improvement when changing the Raman laser intensity from 10% to 100%, the maximum residual frequency shift is 6 kHz. The blue squares are data after improvement, and the frequency shift is less than 500 Hz. The error bars are obtained using Gaussian fitting.

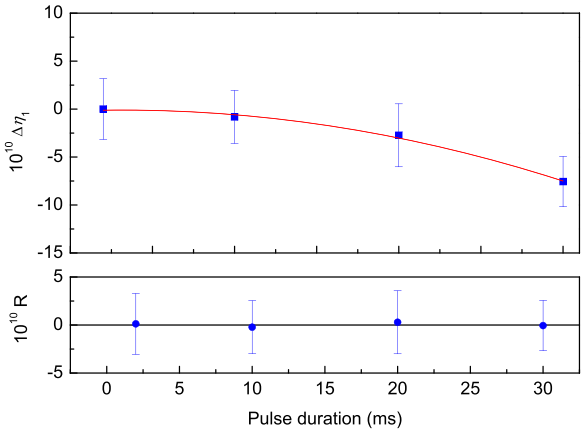

FIG. 6. Dependence of η_1 measurements and their residuals R on the duration of blow away pulse. The blue squares are experimental data, and the red curve is the quadratic polynomial fitting. The error bars are got by the Allan deviation with an integration time of 4480 s or 8960 s. The corresponding value of $\Delta\eta_1$ is fitted as 0.1×10^{-10} at pulse duration of 2 ms. The red dots are residuals, and the black line is the quadratic polynomial fit, the uncertainty of $\Delta\eta_1$ is obtained as 0.2×10^{-10} by the deviation of residuals.

where $\delta_{\text{ac}}^{\text{dw}}$ and $\delta_{\text{ac}}^{\text{up}}$ are ac Stark shifts of the downward part and the upward part of the interference loop at the time of the second Raman pulse. This shift is mainly caused by the residual ac Stark shift associated with the Raman laser intensity gradient. Considering laser beams with a diameter of 30 mm, pulse duration $\tau = 30\,\mu$s, evolution time $T = 203$ ms, and a residual ac Stark shift that is less than 500 Hz, the calculated uncertainty of η caused by the ac Stark shift is less than 0.1×10^{-10}.

To investigate the ac Stark shift of blow away and repumping lasers, we modulate the duration of blow away pulses, and we measure the $\Delta\eta_1$. The ac Stark shift contribution due to blow away lasers is evaluated as 0.1×10^{-10} with an uncertainty of 0.2×10^{-10} (Fig. 6). According to Figs. 3(b), 3(c) and 3(d), the blow away and repumping lasers are different for specific combination pairs, and the corresponding $\Delta\eta$ values are $\Delta\eta_2 = (0.4\pm0.8)\times10^{-10}$, $\Delta\eta_3 = (0.0\pm0.2)\times10^{-10}$, and $\Delta\eta_4 = (-0.1\pm0.2)\times10^{-10}$.

C. Coriolis effect

Due to the horizontal velocity distribution of atom clouds, the Coriolis effect caused by the Earth's rotation couples to the free-falling atoms, so that the fluctuation of position and velocity of atom clouds leads to an uncertainty of η measurement. The Coriolis effect is expressed as

$$\Delta\phi = 2\boldsymbol{\Omega}_{\text{E}}\cdot(\Delta\mathbf{V}_0\times\mathbf{k}_{\text{eff}})T^2, \tag{10}$$

where $\boldsymbol{\Omega}_{\text{E}}$ is the Earth's rotation, and $\Delta\mathbf{V}_0$ is the horizontal velocity difference between two species atom clouds. Since the detectors are fixed, the phase difference mainly depends on the overlap degree of the atom clouds. In our experiments, the Coriolis effect is reduced mainly in two ways: one is to overlap the atom clouds and to reduce atom temperature; the other is to compensate for the rotation of the Raman laser mirror [26,27]. We design and implement [28] a

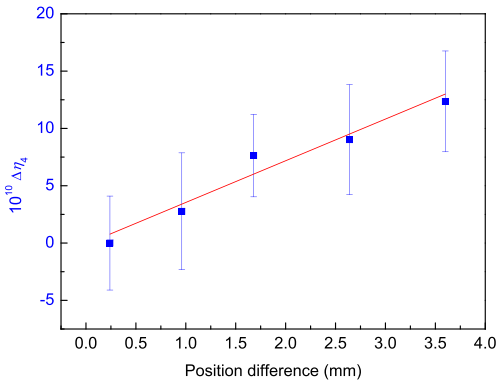

FIG. 7. Dependence of $\Delta\eta_4$ measurements on the position difference of two atom clouds. The velocity difference is 24 mm/s and the interval between velocity-selection pulses for ^{85}Rb and ^{87}Rb is 140 ms. The position difference is 3.36 mm, and the fitting value is $(3.6 \pm 0.5)\times 10^{-10}$/mm. The error bars are obtained by the Allan deviation with an integration time of 4480 or 8960 s.

two-dimensional rotation compensation system for the Raman laser mirror. We perform rotation compensation for the east-west and the north-south direction. The phase responses to the rotation compensation are $\Delta\eta_{\mathrm{E-W}} = 1.1 \times 10^{-9}/\Omega_{\mathrm{E}}$ and $\Delta\eta_{\mathrm{S-N}} = 1.6 \times 10^{-9}/\Omega_{\mathrm{E}}$, and the total residual contribution of the Coriolis effect is $\Delta\eta = (-0.1 \pm 0.4) \times 10^{-10}$.

D. Gravity gradient

The phase shift caused by the position difference between the two atom clouds is [29] $\Delta\phi = k_{\mathrm{eff}} g T^2$, where $\Delta g = T_{zz}\Delta h$, and T_{zz} is the gravity gradient in the z-direction. The center positions of two atom clouds are measured by the time-of-flight (TOF) signal. The trajectory overlap of atom clouds is optimized by adjusting the background magnetic field in the MOT area, the detuning of moving molasses lasers, and velocity selection. We use three sets of pulses for gravity gradient modulation experiments. The first set of pules is for velocity selection of ^{85}Rb and ^{87}Rb atom clouds. The second set of pulses causes ^{85}Rb and ^{87}Rb clouds to obtain recoil velocities in opposite directions, so that their velocity difference is $\Delta\upsilon = 24$ mm/s. The third group of pulses reverses their velocity directions. Thus, we modulate the relative position of two species atom clouds and measure the gravity gradient.

From the linear fitting of the data, the gravity gradient value we obtained is $(3.6 \pm 0.5) \times 10^{-10}$ g/mm, as shown in the Fig. 7, which is slightly larger than the typical value $(3.1 \times 10^{-10}$ g/mm) on the surface of the Earth. The uncertainty of position difference is measured by time fluctuation of the TOF signal as 0.79 mm, and the uncertainty of η measurement corresponding to gravity gradient is 2.8×10^{-10}. The phase shift caused by the velocity difference between the two atom clouds is $\Delta\phi = k_{\mathrm{eff}} T_{zz} \Delta\upsilon_0 T^3$. In our experiment, the velocity uncertainty due to the residual ac Stark shift (< 125 Hz), the quadratic Zeeman shift (< 100 Hz), and the Raman laser frequency difference (< 100 Hz) is less than 100 μm/s. Considering $T_{zz} = 3.1 \times 10^{-7}$g/m and $T = 203.164$ ms, the corresponding phase shift is 6×10^{-12}, which is much smaller than the error of the gravity gradient term.

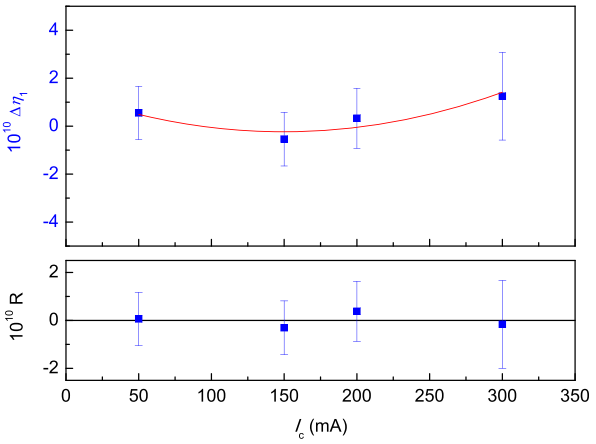

FIG. 8. Dependence of uncertainty of η_1 measurements and their residuals R on the current C-field. The blue squares are measurements using $I_c = 50$, 150, 200, 300 mA. The error bars are obtained by the Allan deviation with an integration time of 4480 or 8960 s. The red line is a fitting curve. The corresponding value of $\Delta\eta_1$ is fitted as 0.5×10^{-10} when the I_c is extrapolated to 320 mA. The red dots are residuals, and the black line is the quadratic polynomial fit. The uncertainty of $\Delta\eta_1$ is obtained as 0.3×10^{-10} by the deviation of residuals.

E. Quadratic Zeeman shift

In ^{85}Rb - ^{87}Rb 4WDR dual-species AI, the phase shift due to the quadratic Zeeman effect is given by

$$\Delta\phi = 2\pi\,(Z_{87-\mathrm{F}} - Z_{85-\mathrm{F}}) \int [B^{\mathrm{up}}(t)^2 - B^{\mathrm{dw}}(t)^2]dt, \quad (11)$$

where I_c is the current of the constant-field coil, which provides a constant magnetic field, $Z_{87-\mathrm{F}}$ and $Z_{85-\mathrm{F}}$ are quadratic Zeeman shift coefficients of ^{85}Rb - ^{87}Rb $|F, m_F = 0\rangle$ states, and B^{up} and B^{dw} are magnetic fields of the downward and upward path, respectively. The quadratic Zeeman shift of ^{85}Rb atoms was measured by Li *et al.* [30]. The Zeeman frequency shift coefficients of the magnetic sublevel of ground fine structure of ^{87}Rb are $Z_{85-1} = -288$ Hz/G^2 (for ^{87}Rb $|F = 1, m_F = 0\rangle$) and $Z_{87-2} = 288$ Hz/G^2 (for ^{87}Rb $|F = 2, m_F = 0\rangle$), while those of ^{87}Rb are $Z_{85-2} = -647$ Hz/G^2 (for ^{85}Rb $|F = 2, m_F = 0\rangle$) and $Z_{85-3} = 647$ Hz/G^2 (for ^{85}Rb $|F = 3, m_F = 0\rangle$). The experimentally measured $\Delta\eta$ values for ^{85}Rb $|F = 2\rangle$ - ^{87}Rb $|F = 1\rangle$ with $I_c = 50$, 150, 200, and 300 mA are shown in Fig. 8. The corresponding value of $\Delta\eta_i$ is fitted by

$$\Delta\phi_{\mathrm{i}}\kappa_{\mathrm{i}} = aI_c^2 + bI_c + c, \quad (12)$$

where

$$\kappa_{\mathrm{i}} = \frac{2k_{\mathrm{eff}} g T^2}{2\pi\,(Z_{87-\mathrm{F}} - Z_{85-\mathrm{F}})}. \quad (13)$$

For $\kappa_1(Z_{87-1}, Z_{85-2})$, we get $\Delta\eta_1 = (0.5 \pm 0.3) \times 10^{-10}$ when the I_c is extrapolated to 320 mA, where the bias value (1.4×10^{-10}) of quadratic polynomial fitting includes the contributions of the zero C-field and other experimental parameters. Since the contribution of the zero C-field (2×10^{-13}) can be ignored, the bias term is deduced from the contribution of a quadratic Zeeman shift.

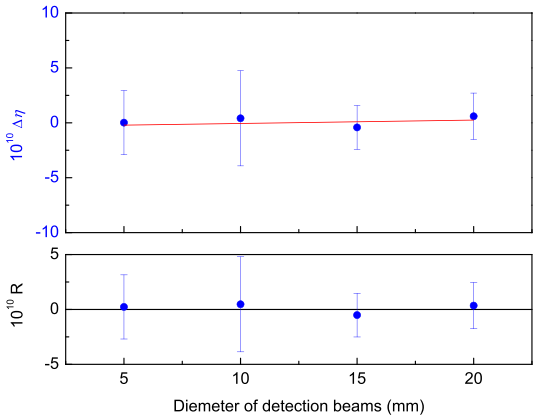

FIG. 9. Dependence of η measurements and their residuals R on the size of detection beams. The blue squares are measurements using a detection beam with a diameter of 5, 10, 15, and 20 mm. The uncertainties of four measurements are all within 1.0×10^{-10}. The error bars are obtained by the Allan deviation with an integration time of 4480 or 8960 s. The corresponding value of $\Delta\eta$ is fitted as 0.5×10^{-10} at a beam diameter of 15 mm. The red dots are residuals, and the black line is the quadratic polynomial fit. The uncertainty of $\Delta\eta_1$ is obtained as 0.5×10^{-10} by the deviation of residuals.

According to Eqs. (12) and (13), the corresponding $\Delta\eta$ values of the other three combination pairs given by using $\kappa_2(Z_{87-2}, Z_{85-2})$, $\kappa_3(Z_{87-1}, Z_{85-2})$, and $\kappa_4(Z_{87-2}, Z_{85-3})$ are evaluated as $\Delta\eta_2 = (1.3 \pm 0.8) \times 10^{-10}$, $\Delta\eta_3 = (-1.3 \pm 0.8) \times 10^{-10}$, and $\Delta\eta_4 = (-0.5 \pm 0.3) \times 10^{-10}$, respectively.

F. Wave-front aberration

We use the expansion-rate-selection method [31] to suppress the phase noise caused by the wave-front distortion of the Raman lasers. The corresponding error due to wave-front aberration is analyzed and estimated by modulation experiments. We use an initial temperature of 3 μK, and detection beam diameters of 5, 10, 15, and 20 mm to measure the wave-front distortion. The experimentally measured $\Delta\eta$ value for $^{87}\mathrm{Rb}\,|F = 1\rangle$-$^{85}\mathrm{Rb}\,|F = 2\rangle$ versus the size of the detection beams is shown in Fig. 9. The actual beam diameter is 15 mm, so the contribution of wave-front distortion is fitted as $(0.5 \pm 0.5) \times 10^{-10}$.

G. Other systematic errors

The errors caused by tides, absolute wavelength of lasers, chirp rate, mirror angle (pointing direction of the Raman beam), and timing control accuracy that are suppressed in 4DWR-e AI are small enough. The collision shift, which depends on the density of the atoms, is also very small under the present condition. The total uncertainty of the contribution of these parameters is 1.0×10^{-10}.

H. Summary

The final data of Eötvös parameters are shown in Fig. 4(c). Fitting with Eq. (5) gives $\eta_0 = (-0.8 \pm 1.4) \times 10^{-10}$, $\eta_E = (0.0 \pm 0.4) \times 10^{-10}$ per reduced energy ratio. The error budget is summarized in Table III.

VI. CONCLUSION

To conclude, we have completed a joint test of the equivalence principle (EP) using atoms with specified mass and internal energy in one experiment. We observed no violation of EP at the 10^{-10} level in the μeV-GeV mass-energy range. The use of a 10-m atomic fountain can realize an atom interferometer with $T \sim 1$ s, and the precision can be improved to 10^{-12} or even better. Compared with the previous tests, this work gives the mass constraint parameter η_0 and the energy constraint parameter η_E simultaneously. The current value of η_E was obtained from a large mass-energy gap experiments. It can be further improved by other mass-energy experiments such as metastable alkaline earth AI at the eV region. The gravity gradient is the main systematic error. To fix this issue, there are two improvements that must be made in the near future. One is to stably control the relative initial position and initial velocity of the two atom clouds by using an optical lattice to coherently accelerate the atoms. Another way is to reduce the influence of the gravity gradient by using recently developed techniques [32,33]. With steady improvements of AI technology, such as the application of high-sensitivity [16] and long-baseline [34,35], fully quantum tests [20,36] of EP will become possible in the future.

ACKNOWLEDGMENTS

We thank Shi-Tong Long, Wen-Dong Zhang, and Jia-Qi Zhong for their contributions to the apparatus or key

TABLE III. Error budget.

	η ($\times 10^{-10}$)				Uncertainty	$\delta\eta$	($\times 10^{-10}$)	
Parameters	η_1	η_2	η_3	η_4	$\delta\eta_1$	$\delta\eta_2$	$\delta\eta_3$	$\delta\eta_4$
Experimental data	49438.1	49437.5	49431.8	49432.7	0.6	1.8	2.5	1.8
Wave vector	49435.6	49436.0	49435.2	49435.6	0.5	0.5	0.5	0.5
ac Stark shift	0.1	0.4	0.0	−0.1	0.2	0.8	0.2	0.2
Coriolis effect	−0.1	−0.1	−0.1	−0.1	0.4	0.4	0.4	0.4
Gravity gradient	0.0	0.0	0.0	0.0	2.8	2.8	2.8	2.8
Quadratic Zeeman shift	0.5	1.3	−1.3	−0.5	0.3	0.8	0.8	0.3
Wave-front aberration	0.5	0.5	0.5	0.5	0.5	0.5	0.5	0.5
Others	0.0	0.0	0.0	0.0	1.0	1.0	1.0	1.0
Total	1.5	−0.6	−2.5	−2.7	3.2	3.7	4.1	3.6

technology. This work was supported by National Key Research and Development Program of China under Grant No. 2016YFA0302002, National Natural Science Foundation of China under Grants No. 91536221, No. 91736311, and No. 11574354, Strategic Priority Research Program of the Chinese Academy of Sciences under Grants No. XDB21010100 and No. XDB23030100, and the Youth Innovation Promotion Association of the Chinese Academy of Sciences under Grant No. 2016300.

[1] C. M. Will, The confrontation between general relativity and experiment, Liv. Rev. Relativ. **17**, 4 (2014).

[2] M. S. Safronova, D. Budker, D. De Mille, D. F. J. Kimball, A. Derevianko, and C. W. Clark, Search for new physics with atoms and molecules, Rev. Mod. Phys. **90**, 025008 (2018).

[3] F. Hofmann and J. Müller, Relativistic tests with Lunar laser ranging, Class. Quantum Grav. **35**, 035015 (2018).

[4] F. W. Hehl, P. von der Heyde, G. D. Kerlick, and J. M. Nester, General relativity with spin and torsion: foundations and prospects, Rev. Mod. Phys. **48**, 393 (1976).

[5] L. Zhu, Q. Liu, H. H. Zhao, Q. L. Gong, S. Q. Yang, P. S. Luo, C. G. Shao, Q. L. Wang, L. C. Tu, and J. Luo, Test of the Equivalence Principle with Chiral Masses Using a Rotating Torsion Pendulum, Phys. Rev. Lett. **121**, 261101 (2018).

[6] P. Touboul, G. Métris, M. Rodrigues *et al.*, MICROSCOPE Mission: First Results of a Space Test of the Equivalence Principle, Phys. Rev. Lett. **119**, 231101 (2017).

[7] L. Koester, Verification of the equivalence of gravitational and inertial mass for the neutron, Phys. Rev. D **14**, 907 (1976).

[8] O. Bertolami and F. M. Nunes, Ultracold neutrons, quantum effects of gravity and the weak equivalence principle, Class. Quantum Grav. **20**, L61 (2003).

[9] S. Fray, C. A. Diez, T. W. Hänsch, and M. Weitz, Atomic Interferometer with Amplitude Gratings of Light and Its Applications to Atom-Based Tests of the Equivalence Principle, Phys. Rev. Lett. **93**, 240404 (2004).

[10] A. Bonnin, N. Zahzam, Y. Bidel, and A. Bresson, Simultaneous dual-species matter-wave accelerometer, Phys. Rev. A **88**, 043615 (2013).

[11] D. Schlippert, J. Hartwig, H. Albers, L. L. Richardson, C. Schubert, A. Roura, W. P. Schleich, W. Ertmer, and E. M. Rasel, Quantum Test of the Universality of Free Fall, Phys. Rev. Lett. **112**, 203002 (2014).

[12] L. Zhou, S. T. Long, B. Tang, X. Chen, F. Gao, W. C. Peng, W. T. Duan, J. Q. Zhong, Z. Y. Xiong, J. Wang, Y. Z. Zhang, and M. S. Zhan, Test of Equivalence Principle at 10^{-8} Level by a Dual Species Double-Diffraction Raman Atom Interferometer, Phys. Rev. Lett. **115**, 013004 (2015).

[13] B. Barrett, L. Antoni-Micollier, L. Chichet, B. Battelier, T. Lévèque, A. Landragin, and P. Bouyer, Dual matter-wave inertial sensors in weightlessness, Nat. Commun. **7**, 13786 (2016).

[14] H. Albers, A. Herbst, L. L. Richardson, H. Heine, D. Nath, J. Hartwig, C. Schubert, C. Vogt, M. Woltmann, C. Lämmerzahl, S. Herrmann, W. Ertmer, E. M. Rasel, and D. Schlippert, Quantum test of the universality of free fall using rubidium and potassium, Eur. Phys. J. D **74**, 145 (2020).

[15] K. Zhang, M. K. Zhou, Y. Cheng, L. L. Chen, Q. Luo, W. J. Xu, L. S. Cao, X. C. Duan, and Z. K. Hu, Testing the universality of free fall by comparing the atoms in different hyperfine states with Bragg diffraction, Chin. Phys. Lett. **37**, 043701 (2020).

[16] P. Asenbaum, C. Overstreet, M. Kim, J. Curti, and M. A. Kasevich, Atom-Interferometric Test of the Equivalence Principle at the 10^{-12} Level, Phys. Rev. Lett. **125**, 191101 (2020).

[17] M. G. Tarallo, T. Mazzoni, N. Poli, D. V. Sutyrin, X. Zhang, and G. M. Tino, Test of Einstein Equivalence Principle for 0-Spin and Half-Integer-Spin Atoms: Search for Spin-Gravity Coupling Effects, Phys. Rev. Lett. **113**, 023005 (2014).

[18] X. C. Duan, M. K. Zhou, X. B. Deng, H. B. Yao, C. G. Shao, J. Luo, and Z. K. Hu, Test of the Universality of Free Fall with Atoms in Different Spin Orientations, Phys. Rev. Lett. **117**, 023001 (2016).

[19] G. Rosi, G. D'Amico, L. Cacciapuoti, F. Sorrentino, M. Prevedelli, M. Zych, Č. Brukner, and G. M. Tino, Quantum test of the equivalence principle for atoms in coherent superposition of internal energy states, Nat. Commun. **8**, 15529 (2017).

[20] R. Geiger and M. Trupke, Proposal for a Quantum Test of the Weak Equivalence Principle with Entangled Atomic Species, Phys. Rev. Lett. **120**, 043602 (2018).

[21] T. Lévèque, A. Gauguet, F. Michaud, F. Pereira Dos Santos, and A. Landragin, Enhancing the Area of a Raman Atom Interferometer Using a Versatile Double-Diffraction Technique, Phys. Rev. Lett. **103**, 080405 (2009).

[22] N. Malossi, Q. Bodart, S. Merlet, T. Lévèque, A. Landragin, and F. Pereira Dos Santos, Double diffraction in an atomic gravimeter, Phys. Rev. A **81**, 013617 (2010).

[23] W. Yang, L. Zhou, S. T. Long, W. C. Peng, J. Wang, and M. S. Zhan, Time-division-multiplexing laser seeded amplification in a tapered amplifier, Chin. Opt. Lett. **13**, 012601 (2015).

[24] G. T. Foster, J. B. Fixler, J. M. McGuirk, and M. A. Kasevich, Method of phase extraction between coupled atom interferometers using ellipse-specific fitting, Opt. Lett. **27**, 951 (2002).

[25] Y. P. Wang, J. Q. Zhong, X. Chen, R. B. Li, D. W. Li, L. Zhu, H. W. Song, J. Wang, and M. S. Zhan, Extracting the differential phase in dual atom interferometers by modulating magnetic fields, Opt. Commun. **375**, 34 (2016).

[26] A. Louchet-Chauvet, T. Farah, Q. Bodart, A. Clairon, A. Landragin, S. Merlet, and F. Pereira Dos Santos, The influence of transverse motion within an atomic gravimeter, New J. Phys. **13**, 065025 (2011).

[27] S. Y. Lan, P. C. Kuan, B. Estey, P. Haslinger, and H. Müller, Influence of the Coriolis Force in Atom Interferometry, Phys. Rev. Lett. **108**, 090402 (2012).

[28] W. T. Duan, C. He, S. T. Yan, Y. H. Ji, L. Zhou, X. Chen, J. Wang, and M. S. Zhan, Suppression of Coriolis error in weak equivalence principle test using ^{85}Rb - ^{87}Rb dual-species atom interferometer, Chin. Phys. B **29**, 070305 (2020).

[29] S. Dimopoulos, P. W. Graham, J. M. Hogan, and M. A. Kasevich, General relativistic effects in atom interferometry, Phys. Rev. D **78**, 042003 (2008).

[30] R. B. Li, L. Zhou, J. Wang, and M. S. Zhan, Measurement of the quadratic Zeeman shift of ^{85}Rb hyperfine sublevels using stimulated Raman transitions, Opt. Commun. **282**, 1340 (2009).

[31] J. G. Hu, X. Chen, J. Fang, L. Zhou, J. Q. Zhong, J. Wang, and M. S. Zhan, Analysis and suppression of wave-front-aberration phase noise in weak-equivalence-principle tests using dual-species atom interferometers, Phys. Rev. A **96**, 023618 (2017).

[32] G. D'Amico, G. Rosi, S. Zhan, L. Cacciapuoti, M. Fattori, and G. M. Tino, Canceling the Gravity Gradient Phase Shift in Atom Interferometry, Phys. Rev. Lett. **119**, 253201 (2017).

[33] C. Overstreet, P. Asenbaum, T. Kovachy, R. Notermans, J. M. Hogan, and M. A. Kasevich, Effective Inertial Frame in an Atom Interferometric Test of The Equivalence Principle, Phys. Rev. Lett. **120**, 183604 (2018).

[34] M. S. Zhan, J. Wang, W.-T. Ni *et al.*, ZAIGA: Zhaoshan long-baseline atom interferometer gravitation antenna, Int. J. Mod. Phys. D **29**, 1940005 (2020).

[35] L. Zhou, Z. Y. Xiong, W. Yang, B. Tang, W. C. Peng, K. Hao, R. B. Li, M. Liu, J. Wang, and M. S. Zhan, Development of an atom gravimeter and status of the 10-meter atom interferometer for precision gravity measurement, Gen. Relativ. Gravit. **43**, 1931 (2011).

[36] M. Zych and Č. Brukner, Quantum formulation of the Einstein equivalence principle, Nat. Phys. **14**, 1027 (2018).